In vivo, in situ and ex vivo comparison of porcine skin for microprojection array penetration depth, delivery efficiency and elastic modulus assessment

Wei, Jonathan CJ; Cartmill, Ian D.; Kendall, Mark AF; Crichton, Michael L.

DOI
10.1016/j.jmbbm.2022.105187

Publication date
2022

Document Version
Final published version

Published in
Journal of the Mechanical Behavior of Biomedical Materials

journal of the mechanical behavior of biomedical materials 130 (2022) 105187

Contents lists available at ScienceDirect

Journal of the Mechanical Behavior of Biomedical Materials

journal homepage: www.elsevier.com/locate/jmbbm

In vivo, *in situ* and *ex vivo* comparison of porcine skin for microprojection array penetration depth, delivery efficiency and elastic modulus assessment

Jonathan CJ. Wei [a,b], Ian D. Cartmill [a], Mark AF. Kendall [a,c], Michael L. Crichton [a,d,*]

[a] Delivery of Drugs and Genes Group (D^2G^2), Australian Institute for Bioengineering and Nanotechnology, The University of Queensland, St Lucia, QLD, 4072, Australia
[b] Department of Biomechanical Engineering, Faculty of Mechanical, Maritime and Materials Engineering, Delft University of Technology, 2628 CD, Delft, the Netherlands
[c] The Australian National University, Canberra ACT, 0200, Australia
[d] Institute of Mechanical, Process and Energy Engineering, School of Engineering and Physical Sciences, Heriot-Watt University, Edinburgh, EH14 4AS, United Kingdom

ARTICLE INFO

Keywords:
Skin
Medical device
Microneedles
Soft tissue biomechanics
Elastic modulus
Histology

ABSTRACT

With the development of wearable technologies, the interfacial properties of skin and devices have become much more important. For research and development purposes, porcine skin is often used to evaluate device performance, but the differences between *in vivo*, *in situ* and *ex vivo* porcine skin mechanical properties can potentially misdirect investigators during the development of their technology. In this study, we investigated the significant changes to mechanical properties with and without perfusion (*in vivo* versus *in vitro* tissue). The device focus for this study was a skin-targeting Nanopatch vaccine microneedle device, employed to assess the variance to key skin engagement parameters – penetration depth and delivery efficiency – due to different tissue conditions. The patches were coated with fluorescent or ^{14}C radiolabelled formulations for penetration depth and delivery efficiency quantification *in vivo,* and at time points up to 4 h *post mortem.* An immediate cessation of blood circulation saw mean microneedle penetration depth fell from ~100 μm to ~55 μm (~45%). Stiffening of underlying tissues as a result of *rigor mortis* then augmented the penetration depths at the 4 h timepoint back to ~100 μm, insignificantly different ($p = 0.0595$) when compared with *in vivo*. The highest delivery efficiency of formulation into the skin (dose measured in the skin excluding leftover dose on skin and patch surfaces) was also observed at this time point of ~25%, up from ~2% *in vivo*. Data obtained herein progresses medical device development, highlighting the need to consider the state and muscle tissues when evaluating prototypes on cadavers.

1. Introduction

For microscale medical devices interacting with the skin, it is important to understand how biological tissues affect the performance of the devices – such as their ability to penetrate and deliver drugs. It is evident that the factors affecting dynamic device-skin interaction are beyond skin deep – often requiring to consider fat, muscle and bone as the complete system (Shankar et al., 2014). Underlying tissues are also likely to contribute to data scatter (Wei et al., 2017), and furthermore, we must ask how the *in vivo* condition differ from the *ex vivo* experiments carried out, where fat, muscle and bone are isolated/separated. This question is not trivial – the differences between *in vivo*, *in situ*, and *ex vivo* conditions could cause substantial device performance variations. Beyond simple layer inclusion, the presence of systemic circulation of blood and other fluids in the body – known as perfusion – *in vivo* also adds to comparison complexities. This circulation does not exist *in situ*, or *post mortem*, and *ex vivo* (or *in vitro* depending on literature). It has been proposed (Bilston, 2002) on various soft tissues that perfusion (and *ex vivo* boundary conditions) influences the overall mechanical properties of soft tissues, such as liver, brain and gastrointestinal organs.

Comparing tissues of all three states is a significant undertaking; hence limited data are available in the literature, for various soft tissues, let alone skin (Guertler et al., 2018). Indicated in Guertler et al.'s publication (Guertler et al., 2018) that the comparison between *in vivo, in situ* and *ex vivo* porcine brain tissues would be of interest, however, logistical challenges would be substantial. In this paper, we characterise porcine skin in all three states. This is a challenge due to the mechanically complex material composition, in comparison to the more

* Corresponding author. Institute of Mechanical, Process and Energy Engineering, School of Engineering and Physical Sciences, Heriot-Watt University, Edinburgh, EH14 4AS, United Kingdom.
E-mail address: m.crichton@hw.ac.uk (M.L. Crichton).

https://doi.org/10.1016/j.jmbbm.2022.105187
Received 20 December 2021; Received in revised form 13 March 2022; Accepted 17 March 2022
Available online 25 March 2022

homogeneous brain and liver tissue (Lister et al., 2011) –skin is anisotropic, multi-layered with distinct physical and mechanical properties. Moreover, as with other medical devices (e.g. the biolistic gene gun (Kendall et al., 2004a; Kendall et al., 2004b)), various microneedle mediated drug delivery studies published in the last few decades are often carried out on excised tissues (*ex vivo*) or *in vivo* animal models (Birchall, 2006), making comparisons difficult.

Animal and human cadavers are commonly used in research, for reasons such as tissue availability, cost and ethical considerations, however, changes to a body after death occurs in several stages during the *post mortem* interval (PMI), which can alter tissue properties. In brief, *pallor mortis* is the first stage of death, resulting from the termination of capillary circulation. Then, the sinking of blood to the bottom of the body is known as *livor mortis*. *Algor mortis* is the cooling of the body, which can, for instance, reduce diffusion rates for experiments (Raphael et al., 2013; Wei, 2018). The transient behaviour of the stiffening of muscles due to chemical changes is known as *rigor mortis*. Its onset and duration depend on the body size and species, temperature of the environment, which has resulted in onset and cessation of between 3 and 36 h *post mortem* (Brooks, 2016). Although *rigor mortis* has been extensively studied in the meat industry to improve the texture of its products (Davey et al., 1976), how tissue stiffening alters the mechanical properties is not well known. Furthermore, whether this affects the skin's mechanical properties *in situ* remains unknown. This is therefore important for applications beyond microneedle device testing – for instance in evaluating robotic surgical tools. The closest body of work performed in this field was by Groves (Groves et al., 2012), who measured murine and human skin differences and performed an inverse finite element modelling (FEM) on various skin conditions, with the exception to the *in situ* condition, using 700 μm long steel and 280 μm long silicon microneedles. The author further reported *in vivo* and *ex vivo* puncturing of both murine and human skin with microneedles applied quasi-statically by hand. Difficulty in penetrating mouse skin was observed, while *ex vivo* human skin was breached with high loads (4–5 N), although the author remarked on the difficulty in characterising *in vivo* punctures.

Given the above, this manuscript seeks to identify how representative porcine skin is *in vivo* clinical conditions with *ex vivo* or *in situ* conditions. In particular, for microtechnology development, we are interested whether simple correction factors can allow indirect comparison between tissue states. Therefore, the purpose of this paper is to identify potential differences between the conditions, from a medical device standpoint, and the implications of evaluating these devices on these models to progress on preclinical research by establishing a reference between different states.

In this work, we take a device-focussed approach, with two main parameters characterising delivery of formulation into skin using a prototype Nanopatch (microarray patch) device. First, penetration depth measurements provide quantitative information on the depth the microprojections can reach in the tissue. Second, a radiolabelled formulation is used to assess the fraction of formulation released into the skin as delivery efficiency. This work complement our previous measurement of *in vivo*, and *in situ* skin elastic modulus (Cartmill, 2014). A non-invasive measuring technique was then developed for this task, based on other established methods like air-jet indentation (Chao et al., 2010) and water-jet indentation (Huang et al., 2009). We hypothesised that the elastic modulus of skin, together with the underlying tissue layers will change *post mortem*, will significantly alter the penetration depth and delivery efficiency of the Nanopatch. In this study, all three parameters were measured *in vivo* on pigs and repeated at several time-points post-euthanasia.

2. Materials and methods

2.1. Ethics statement

All animal work carried out has been approved by The University of Queensland Animal Ethics Committee (approvals AIBN146/13/VAX-XAS, AIBN/556/12/ARC/NHMRC/SMART (33)). All experiments were carried out in accordance with The University of Queensland guidelines and regulations.

2.2. Animal model

Seven Large White breed pigs were used in this study. Experiments were carried out following other researchers' studies, and no additional animals were used, adhering to the 3R principle for animal use from the UQ guidelines. Pigs 1–2 were housed at the Queensland Animal Science Precinct (QASP, Gatton QLD, Australia) and pigs 3–7 at the Herston Medical Research Centre (HMRC, Herston QLD, Australia). All except pig 2 were female, average mass 34.8 ± 7.4 kg, average age 4 months ±2 weeks old. Hair from the skin was shaved using animal hair clippers (Pet grooming kit, Wahl, Stirling IL, USA). Pigs were euthanised by pentobarbital injection (Lethabarb, Virbac, Carrros, France). Rump site was chosen because of its ease of access (vs. e.g. inguinal region), relatively flat and large area, deep layer of consistent soft tissues with no bones immediately beneath the skin.

2.3. Experimental design

Key indicators to assess medical device performance on different tissue states (*in vivo* and *in situ*), in this case, the microneedles, are microprojection penetration depth (PD) and formulation delivery efficiency (DE). This data was gathered from two pigs before and after euthanasia. Time points were selected as immediately prior to euthanasia (t = 0), immediate after (t = 10 min), and at 30 and 60 min. Further investigations on longer time points of 120 and 240 min were carried out on pigs 3–5 after the analysis on the data of pigs 1–2. *Ex vivo* conditions with completely excised skin and synthetic backing material were carried out on pigs 5–7. Experiments were carried out in a separate room inside the animal housing facility. Air conditioning was turned on at the start of the experiment set to approximately 25 °C. Elastic modulus data was also obtained from non-invasive skin-surface perturbations captured from high-speed video footage carried out in conjunction with an earlier study with pigs 1–4 [17] reported.

2.4. Nanopatch manufacture

Nanopatch wafers were patterned and made from 2 mm thick, six-inch silicon wafers using the deep reactive-ion etching (DRIE) process at the Australian National Fabrication Facility, Queensland Node (ANFF-Q, Brisbane QLD, Australia), as per previous studies (Crichton et al., 2016; Jenkins et al., 2012). In brief, patches were manufactured with hexagonally patterned smooth-convex shaped projections of ~230 μm in length, ~40 μm base diameter, at a high density of 10,000 projections per cm^2, and diced into 4 × 4 cm squares (Fig. 1 (a)). This prototype design and construction extends beyond Nanopatch prototypes applied to deliver vaccines to thinner rodent skin – such as mice (Chen et al., 2012; Ng et al., 2012; Fernando et al., 2016) and rats (Muller et al., 2016, 2017).

2.5. Nanopatch coating

Coating formulation and approaches were similar to our previous work (Crichton et al., 2016; Chen et al., 2009). Briefly, coating formulation were deposited onto the projection surfaces and blow-dried. Formulation comprises methylcellulose (M0387, Merck, Darmstadt, Germany), flu vaccine (Fluvax 2014; CSL, Parkville VIC, Australia),

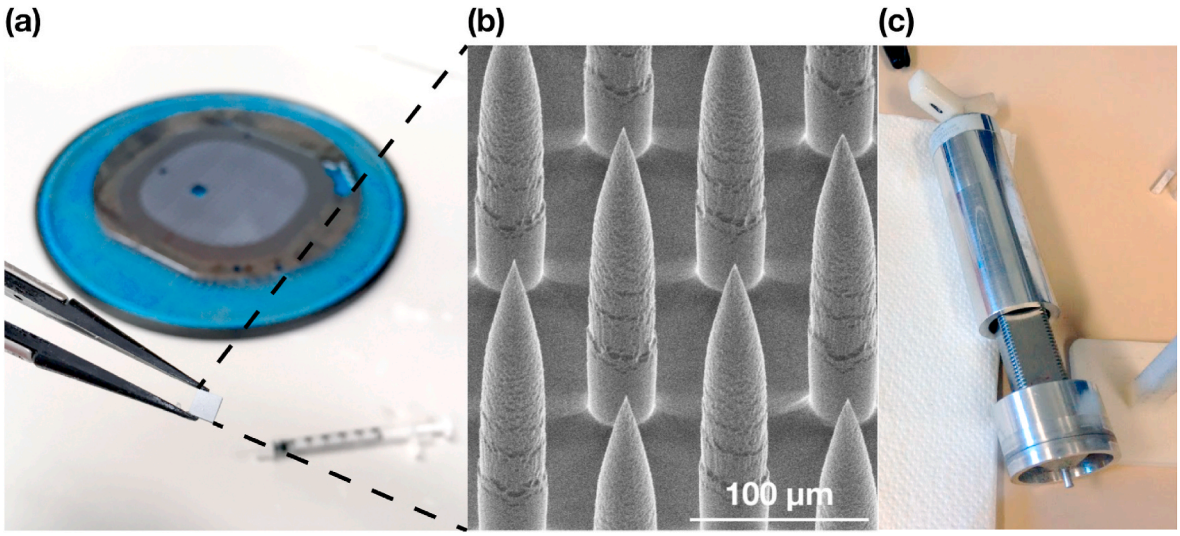

Fig. 1. (a) A Nanopatch held with tweezers, diced Nanopatch wafer and a syringe in the background for size comparison. (b) SEM image of Nanopatch projections viewed from 45° and (c) the applicator device.

Dulbecco's phosphate buffered saline (DPBS) (D8662, Merck, Darmstadt, Germany) and either Coomassie blue dye (161–0400, Bio-Rad, Hercules CA, USA) with ^{14}C-labelled ovalbumin (ARC 0431, American Radiolabeled Chemicals, St Louis MO, USA) for delivery efficiency studies, or FluoSpheres fluorescence (F8811, Thermo Fischer Scientific, Waltham MA, USA) for penetration depth imaging.

2.6. Nanopatch imaging

Nanopatch surface morphologies after etching were viewed under scanning electron microscopy (SEM) using the Jeol Neoscope (JCM-5000, Jeol, Tokyo, Japan) at 10 kV tilted at 45°, as shown in the representative image in Fig. 1 (b).

2.7. Nanopatch applicator manufacture and calibration

Extending upon previous spring-based applicators of Nanopatch used in mice (Crichton et al., 2010), a spring-loaded Nanopatch applicator, shown in Fig. 1 (c), was manufactured featuring the ability to adjust the patch application velocity by changing the spring compression distance with Hooke's law, $F = kx$ and relating it to the spring potential energy, $E_P = \frac{1}{2}kx^2$ and kinetic energy, $E_K = \frac{1}{2}mv^2$. Spring constant was provided by the manufacturer datasheet as 1236 N m^{-1} (LC 055H 12, Lee Spring, Wokingham, United Kingdom). The applicator was calibrated using a high-speed camera (FastCam SA4, Photron, San Diego CA, USA) observing the plunger velocity. Application velocities of 8, 12 and 16 m s^{-1} were estimated with a total approximate E_K of 1.05, 2.37 and 4.21 J respectively. The applicator plunger was designed to be arrested after the patch contacted the skin, and most of the energy was not transferred to the skin. Insights into the bio-viscoelasticity of skin at both the micro-scale and strain-rate of interest (Crichton et al., 2010, 2013; Kendall et al., 2007) led to a lower-energy 'flying patch' concept (Goddard et al., 2018) that has been applied to Nanopatch clinical studies (Fernando et al., 2018).

2.8. Patch application for penetration depth on in vivo and in situ skin

The handheld applicator was first adjusted for spring compression to 16 m s^{-1} and then loaded with a Nanopatch, applied steadily onto the selected site free of visible scarring and defects. A schematic of the applicator is shown in Supplementary Fig. 1(a and b). Three ^{14}C-coated patches and two fluorescence-coated patches were applied per condition per pig. Each patch took approximately 30 s to apply and was patched on one side of the pig. Patches were left on the skin for 2 min before removal to allow sufficient time for the coating formulation to elute into the skin. Patched areas were marked and excised at the completion of all patch applications. Patched sites were excised with an approximate 1 mm border.

2.9. Patch application for penetration depth on ex vivo skin

Rump skin was excised from pigs 5–7. Naïve skin samples from these pigs were measured for a previous study (paper, sup) and were found to be statistically similar for those two sites. Freshly excised skin with subcutaneous tissue was pinned using hypodermic needles on three 10 mm thick polydimethylsiloxane (PDMS) (Sylgard 184, Dow Corning, Midland MI, USA) sheets at a 10:1 PDMS to the crosslinking agent, cured at 80 °C for 4 h, to simulate uniform subcutaneous and muscle tissues. The skin was marked prior to excision and pinned back to its original dimensions to mimic its original *in vivo* tension, shown in Supplementary Fig. 1 (c). The experiment was carried out indoor as per other experiments with the skin temperature stabilised to room temperature. Patches were applied as per above at predetermined spring compression lengths representing application velocities of 8, 12 and 16 m s^{-1}. Patched areas were subsequently excised for histology and imaging. Photos of patched area overview were taken using an iPhone 6 (Apple, Cupertino CA, USA) in Fig. 4(d–h). Other photos were taken with an iPhone SE. Images were cropped, rotated, adjusted globally for tone, contrast and colour using the Auto function in Photoshop CC (Adobe, San Jose CA, USA).

2.10. Histology, microscopy and measurement of penetration depth

Histology sections were obtained using methods similar to past studies (Wei et al., 2017). In brief, skin was fixed and rinsed in neutral buffered formalin (NBF) 10% (HT501128, Merck, Darmstadt, Germany) and phosphate buffered saline (PBS) 1x (mix of Merck, Darmstadt, Germany and Thermo Fischer Scientific, Waltham MA, USA) and embedded in sectioning matrix (Tissue-Tek OCT, Sakura Finetek, Aalphen aan den Rijn, The Netherlands) then frozen with liquid nitrogen. Samples were held upright during freezing to ensure tissues are perpendicular to the cutting plane. Skin specimens were cut perpendicularly across its thickness at ~14–20 μm sections using the Microm HM 560 cryostat (Thermo Fischer Scientific, Waltham MA, USA). Each section was not immediately adjacent to each other as to obtain more representative samples (approx. 350 μm of specimen was discarded

between each section). Samples were not stained as multiphoton microscopy was used to measure the skin layer thicknesses (described in more detail below). The method to measure the thicknesses follows an earlier study (Wei et al., 2017). Images shown in Fig. 4 were shown rotated and cropped in Photoshop CC.

2.11. Multiphoton microscopy

Sectioned samples were viewed under the Zeiss LSM 510 Meta multiphoton microscope (Zeiss, Oberkochen, Germany) using the Plan-Apochromat 10x/0.45 M27 objective. Specimens were excited using 5% 840 nm and 22% 488 nm lasers. Collagen was collected using 390–464 nm IR filter (pseudo-coloured as blue in Fig. 4(a–c)); Fluo-Spheres were filtered using 500–550 nm IR filter (pseudo-coloured as green). Approximately 100 penetration tracks were measured for each specimen, subjected to sample quality. Measurements were taken using the microscope's supplied software, Zen (Zeiss, Oberkochen, Germany).

2.12. Quantification of delivery efficiency

The delivered dose of coating formulation into skin comparing *in vivo* and *in situ* conditions was quantified as per previous studies using ^{14}C-labelled ovalbumin (Pearson et al., 2013). In brief, patches were applied as per above, left on for 2 min and removed. Skin surface was swabbed with cotton earbuds to analyse formulation left on the surface. The skin was excised after all patches have been applied. Delivery efficiency was calculated as the fraction of ^{14}C deposited into the skin, over the total ^{14}C formulation remaining on the patch, skin surface and in the skin.

2.13. Measurement of approximate elastic modulus of the skin

Skin elastic modulus was estimated using Rayleigh wave propagation method (Kendall et al., 2004c) whereby we model the skin (and soft tissue in general) a semi-solid material which behaves like a fluid in several respects (Kirkpatrick et al., 2004; Zhang and Greenleaf, 2007; Li and Oldenburg, 2011; Zhang et al., 2011; Guan et al., 2014; Manfredi et al., 2012), and has been used in diagnostic applications, in for example, skin cancer and scleroderma identification (Li et al., 2011). The wave propagation when the patch impacts the skin was captured using a same high-speed camera (FASTCAM SA4, Photron, Tokyo, Japan) pointed at approximately 45° to the skin surface with a tungsten light source (Lilliput 650 W, Ianrio, Taipei, Taiwan). A black line is drawn across the area where the patch will impact for the camera to capture the wave amplitude. The video footage (see Fig. 2) was analysed in Matlab (MathWorks, Natick MA, USA) to trace the black line and thus extract the wave amplitude and propagation speed. Three patches per time point were used. The patches were 10 × 10 mm in clear polycarbonate plastic (for the drawn line to be visible for the camera) applied using the same method as above. This patch method was first validated in an *in vitro* silicone-based polydimethylsilane (PDMS) sheet model vs. indentation method producing an error of approximately 5%.

The derivations briefly: the Rayleigh wave method is described by Guan et al. (2014) using a modified Voigt model with mass in Equation (1) to estimate the coefficients of shear movement:

$$F(t) = kx(t) + \mu \frac{d}{dt}x(t) + m\frac{d^2}{dt^2}x(t) \quad (1)$$

where $F(t)$ is the applied impuse force, $x(t)$ is the induced shear displacement at the testing point, k is the tissue stiffness, μ is the viscous damping coefficient and m is the mass. As the mass of the vibrating tissue will generally be unknown here, the authors propose the use of relative parameters to indicate the viscoelasticity of the skin:

$$\frac{k}{m} = \omega_n^2, \frac{\mu}{m} = 2\zeta\omega_n \quad (2)$$

where ω_n is the natural frequency and ζ is the viscous damping ratio. Then, the governing equation for wave propagation in an infinite isotropic medium may be written as follows (Zhang et al., 2011):

$$(\lambda + 2\mu)\nabla\nabla\cdot\mathbf{u} + \mu\nabla^2\mathbf{u} - \rho\frac{\partial^2\mathbf{u}}{\partial t^2} = 0 \quad (3)$$

where $\mathbf{u}$ represents the displacement vector, ρ is the mass density, and λ and μ are the Lamé constants of the relevant medium (μ is the shear modulus G). Equation (3) has been solved in a cylindrical polar coordinate system and results in the following relationship between surface wave speed and shear modulus, assuming incompressibility and thus a Poisson's ratio of 0.5 for human tissue (Zhang and Greenleaf, 2007; Zhang et al., 2011):

$$C_R = \frac{C_{shear}}{1.05} = \frac{1}{1.05}\sqrt{\frac{G}{\rho}} \quad (4)$$

where C_{shear} is the shear wave velocity. Converting from shear to the elastic modulus E, and expanding the expression to explicitly include the relationship to Poisson's ratio ν, a relationship between surface propagation speed and E in an isotropic, homogenous material can be derived (Li et al., 2011):

$$C_R = \frac{0.87 + 1.12\nu}{1+\nu}\sqrt{\frac{E}{2\rho(1+\nu)}} \quad (5)$$

where C_R is the wave propagation speed and ρ is the density. The depth of the surface wave motion is proportional to the wavelength with the result that the effective probing depth of the wave z can be estimated by

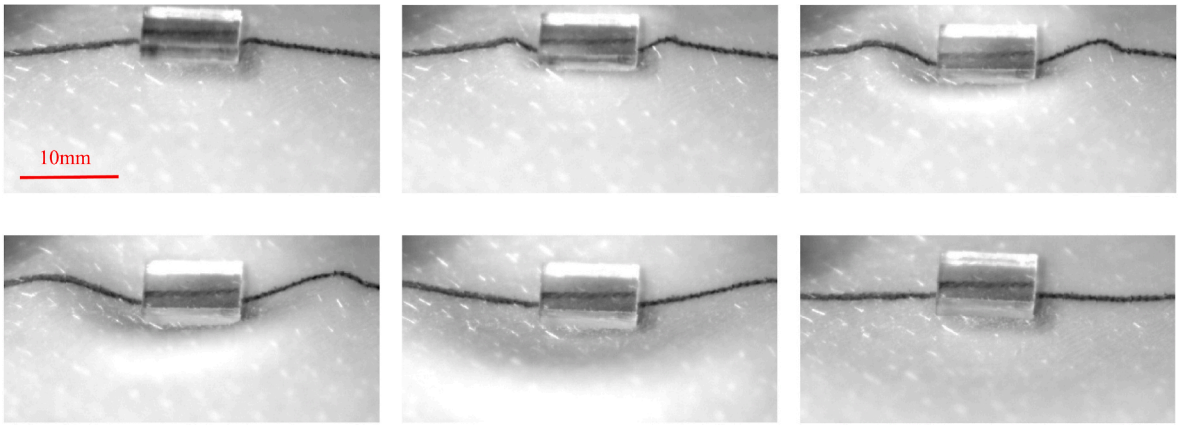

Fig. 2. Polycarbonate 10 × 10 mm patch impacting pig inguinal skin (total elapsed time ~9.5 ms).

the relation (Li et al., 2011):

$$z \approx \lambda = \frac{C_R}{f} \quad (6)$$

where f is the wave frequency. It was suggested that the relevant equations for the surface wave method are generally local and do not require boundary conditions if wave reflections can be ignored (Zhang and Greenleaf, 2007; Zhang et al., 2011).

2.14. Measurement of temperatures

An infrared temperature gun (800101, Sper Scientific, Scottsdale AZ, USA) was used to determine the skin surface temperature at the patching surface just prior to each patch application. The same sensor was also used to determine ambient temperature.

2.15. Statistical analysis

Penetration depth comparisons were performed in Prism (GraphPad, La Jolla CA, USA) using the Kruskal-Wallis test/Dunn's multiple

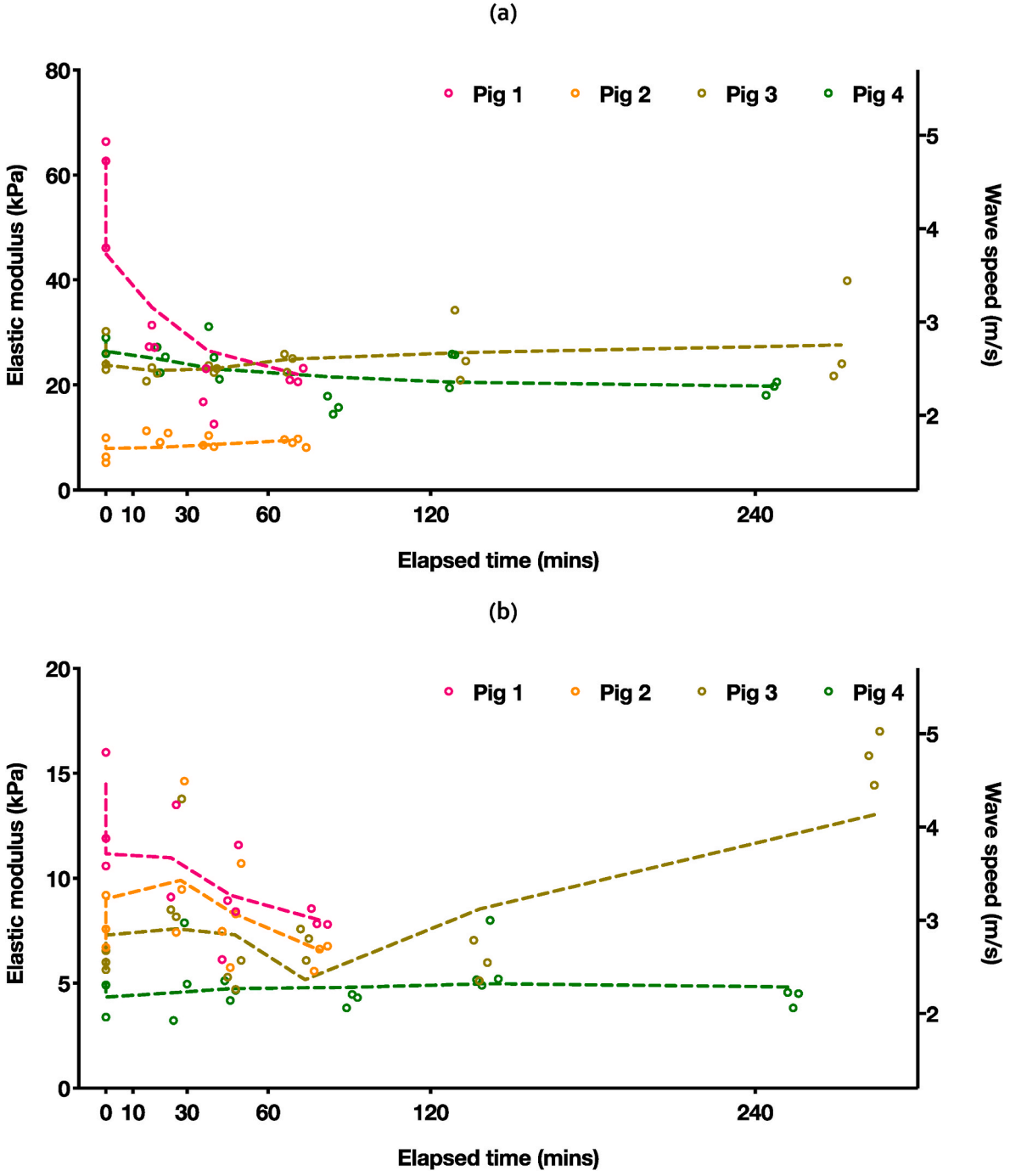

Fig. 3. (a) Inguinal and (b) rump skin elastic modulus obtained from Rayleigh wave perturbations over time post euthanasia (t = 0 prior) for individual pigs. Dotted lines are smooth curves fitted to the mean of each time point and pig number. The corresponding approximate wave speeds are shown on the right y-axis. Two extra time points were carried out on pigs 3 and 4.

comparisons test, due to the time points such as 240 min resembling a bimodally distributed dataset. Mean porcine skin elastic moduli between time points was compared using ordinary one-way ANOVA/Sidak's/Dunn's multiple comparisons test. Mean elastic modulus of human forearm and ^{14}C were compared using ordinary one-way ANOVA/Tukey's multiple comparisons test. Ballistics gel elastic modulus between the flying patch method and indentation was compared using unpaired *t*-test. Exponential and linear curves for penetration depths *versus* velocity were fitted in Matlab R2017.

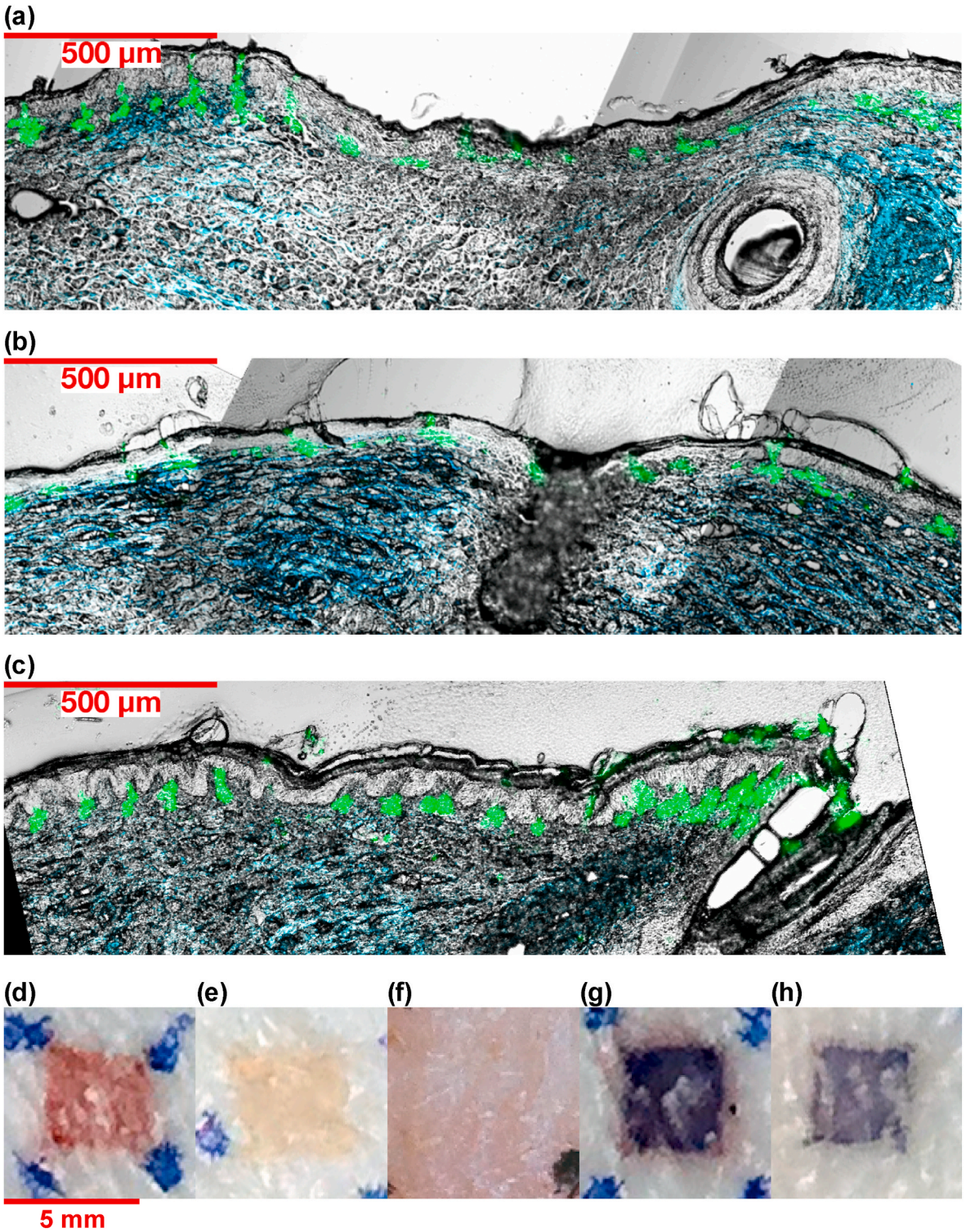

Fig. 4. (a) Tiled images of the representative patched site of *in vivo* porcine rump. Penetration tracks marked with formulation released into rump skin were shown pseudo-coloured as green, while collagen is shown as blue, marking the dermis layer. (b) *In situ* tissue (t = 10 min) of the same site and (c) *ex vivo* tissue. Representative images of patched sites: (d) *in vivo*, FluoSpheres coated patch; (e) *in situ*, FluoSpheres coated patch; (f) *ex vivo*, FluoSpheres coated patch; (g) *in vivo*, ^{14}C and Coomassie blue coated patch; (h) *in situ*, ^{14}C and Coomassie blue coated patch. Blue or black dots on patched corners are permanent marker markings. (For interpretation of the references to colour in this figure legend, the reader is referred to the Web version of this article.)

3. Results

To compare potential tissue properties affecting device performance, penetration depth of microprojections and delivery of formulation coating on the Nanopatch was measured. A comparison was made on *in vivo*, *in situ* and *ex vivo* porcine rump skin. The controlled targeting of skin layers was also shown by adjusting the application velocity. Elastic modulus data of the same conditions and time points were also collected using a non-invasive method.

3.1. Elastic modulus between in vivo and in situ porcine skin

Of the four pigs studied for the change in bulk skin elastic modulus over time past euthanasia, pig 1 prominently showed a significant decrease in elasticity immediately after euthanasia (from ~60 kPa to ~20 kPa), but not for the other pigs (~20–30 kPa for all time points). Besides comparing the 10, 30 and 60 min time point of pig 1, no statistical significance was also calculated for any other comparisons of each pig. A higher spread of elastic modulus was observed in pig 3's final time point of 240 min, but not significantly different from other time points. Interestingly, the same experiment repeated on inguinal skin tissue showed no statistical significance in tissue elastic moduli before and immediately after euthanasia. Pig 3 inguinal tissues showed significantly increased elastic moduli at the final time point at 240 min in Fig. 3 (a), and rump tissue as a comparison in (b).

3.2. Penetration observations of micro-projections into the porcine skin between in vivo, in situ and ex vivo tissues

Fluorescence-conjugated formulation deposited in skin shown in Fig. 4(a–c) clearly illustrates the depths the projection tips reached. For *in vivo* skin, several projections reached into past the dermal-epidermal junction into the papillary dermis, while the projections in the *in situ* condition appeared to have mostly reached the dermal-epidermal junction. Compared to *ex vivo* skin using the same application velocity, the formulation deposition marks also appeared uniform, reaching just past the dermal-epidermal junction. The reduction in penetration depth post-death was also reflected on the quantitative data (n ~100 at each time point for each pig), where the measured depths of the projections shown in Fig. 5 indicated an immediate drop in mean penetration depth and spread from 97 ± 37 μm to 54 ± 27 μm at t = 10 min post-euthanasia. The mean penetration gradually increased over time, recording a mean depth of 74 ± 21 μm at 30 min, 79 ± 26 μm at 60 min, 81 ± 24 μm at 120 min and 95 ± 47 μm at 240 min, which is statistically insignificant between 0 and 240 min ($p = 0.8723$). *Rigor mortis* was observed in pigs 3 and 5 at the final time point of 240 min (a factor of ambient temperature, shown in Supplementary Fig. 3). The penetration depth was shown in Fig. 5 increasing past the dermal-epidermal junction, as opposed to pig 4, whose penetration measurements remained primarily in the viable epidermis.

Comparing with *ex vivo* skin of the same application speed, this was measured as 79 ± 23 μm, which was remarkably similar to the *in situ* conditions prior to *rigor mortis*. P-values of the penetration depth comparisons can be found in Supplementary Table 1. The inter-specimen variability of *ex vivo* skin shown in Fig. 6 is significantly tighter than the *in vivo* counterparts. Once projections breached through the dermal-epidermal junction, the spread of dermis penetration appeared to be greater than the lower speed settings.

Redness of tissue or erythema was observed for *in vivo* patched sites only. This was not observed for *in situ* and *ex vivo* tissues, shown in Fig. 4 (d–h). The fluorescence-coated formulation can be seen deposited into the skin in (e) in the absence of erythema, however it is not as visible as with the *ex vivo* condition (d). Coomassie blue in formulations (g-h) provided a visual assessment of the delivery, illustrating consistent delivery (surface coverage) of formulations into both *in vivo* and *in situ* tissue.

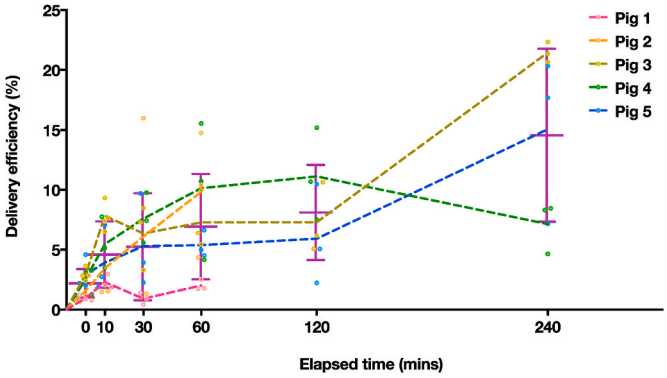

Fig. 6. (a) Combined pigs 1–5 of coating formulation delivered into the skin at each time point post euthanasia (t = 0 prior) on the rump. Mean trend lines are also shown for each pig. Note that extra two time points were carried out on pigs 3–5.

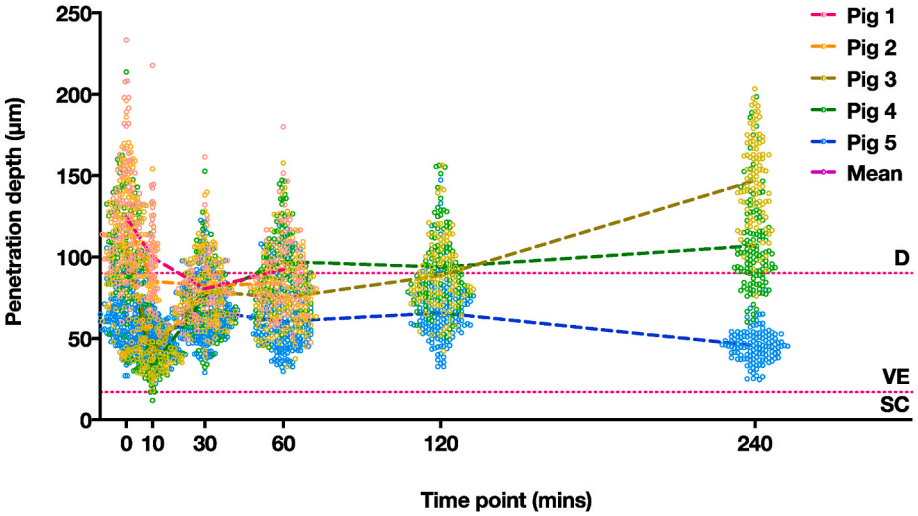

Fig. 5. Measured penetration depths for pigs 1 through 5 at each time point post euthanasia (t = 0 prior) on the rump (n ~100 for each pig at each time point). Mean trend lines are also shown for individual pigs. Note that extra two time points were carried out on pigs 3–5.

3.3. Penetration depths of varying application velocities on ex vivo porcine skin

The penetration depth counts of microprojections (Fig. 1) obtained from histology sections (Fig. 4) are shown in Fig. 7 (a). Controlled skin layer targeting was observed by the adjustment of application velocity. Penetration depth increased proportionally with application velocity. An exponential curve fitted to the dataset passing through the origin ($y = 3.608x^{1.106}$) suggests, the proportionality appeared approximately linear in this range, and a straight trend line was also obtained ($y = 4.766x$), although this assumes the skin is homogenous. The mean penetration depths were 40 ± 15 μm, 50 ± 15 μm and 70 ± 23 μm for application velocities of 8 m s^{-1}, 12 m s^{-1} and 16 m s^{-1} respectively – a 20 μm difference between 12 m s^{-1} and 16 m s^{-1}, and 10 μm difference between 8 m s^{-1} and 12 m s^{-1}. Data points were mostly scattered in the deeper viable epidermis, past the dermal-epidermal junction and into the papillary dermis only for the 16 m s^{-1} condition. The penetration data of the lower speed conditions were mainly recorded in the VE. Corresponding skin layer thicknesses are also shown in the subfigures of Fig. 4 at different sites.

3.4. Delivery of formulation into the porcine skin between in vivo and in situ tissues

Quantitative data in Fig. 6 revealed that delivery efficiency increased post-death, from an average before death of 2.2 ± 1.2%, rising to 4.6 ± 2.8%, 5.3 ± 4.5% and 6.9 ± 4.4% by the end of the hour and 8.1 ± 4.0% by the end of the second hour. The later additional time points carried

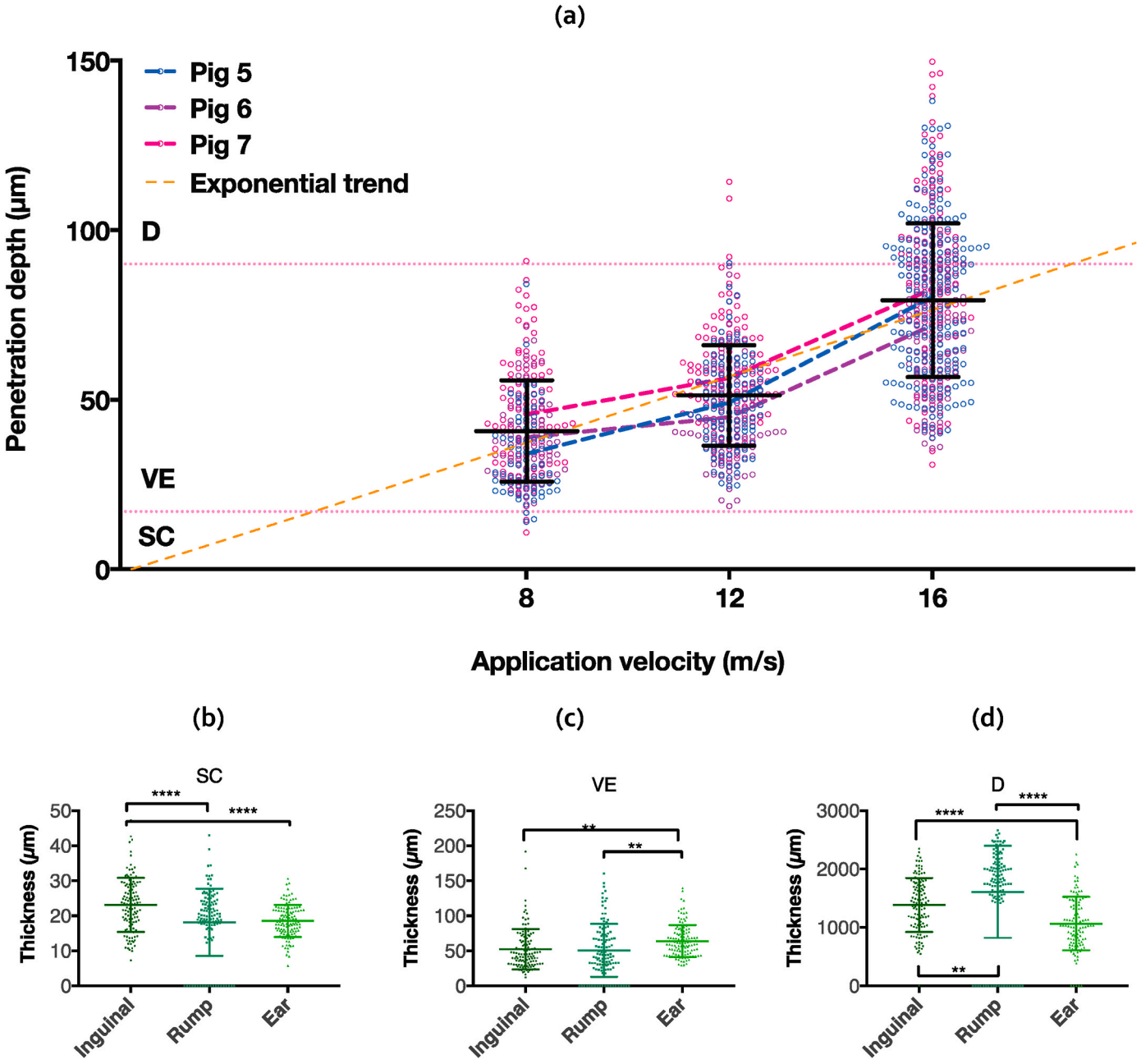

Fig. 7. (a) Measured penetration depths of *ex vivo* skin, tested at 8, 12 and 16 m s^{-1} patch application speed. The exponential curve fitted to the dataset shown in dotted orange line through the origin. Mean trend lines were also shown for each pig. Comparison between pig inguinal, rump and ear skin layer thickness (b) of stratum corneum (c) viable epidermis and (d) dermis, taken along with the penetration depth samples. (For interpretation of the references to colour in this figure legend, the reader is referred to the Web version of this article.)

out on pigs 3–5 showed that of the two (#3, #5) that exhibited *rigor mortis* at the 4 h time point, corresponding to a delivery of 18.3 ± 5.6%, whereas the one without *rigor mortis* was significantly less at 7.1%, similar to previous time points. Statistical significance was only reported for t = 0 *versus* 60, 120 and 240 min; t = 10, 30, 60 and 120 *versus* 240 min.

4. Discussion

The field of microdevices for drug/vaccine delivery, wearable technology and clinical devices relies heavily on the use of animal models for pre-clinical work. Within this paper we sought to understand the differences between tissue states affecting microscale medical device performance (with a focus on penetration depth and delivery efficiency). This body of work showed, for the first time, the states of live and death can affect the quantity of drug delivery and puncture depth of such a technology.

4.1. Differences in the elastic modulus of the skin in vivo, in situ and ex vivo

Whilst previous work has assessed the elastic modulus of porcine liver (Brown et al., 2003) and brain (Gefen and Margulies, 2004; Prevost et al., 2011) skin had not been similarly studied. The results reported in those studies are in sharp contrast to the data arisen herein – that is, the skin elasticity appeared to be lower *in situ*, compared to *in vivo* condition (Fig. 3). This was reflected in the penetration depth data (Fig. 5), but not the delivery efficiency data (Fig. 6). However, a recent publication by Guertler et al. reported agreement with this study: porcine brain tissue was stiffer *in vivo* than *ex vivo*, although only in high frequency-perturbations of 100–125 Hz (Guertler et al., 2018), not unlike the dynamic method of patch application used herein. Groves (Groves et al., 2012) investigated *in vivo* and *ex vivo* murine and human skin, and identified significant differences between the two conditions for microneedle penetration, who hypothesised that this was influenced by subcutaneous fat. Therefore, it is important that the underlying strata of an *ex vivo* model feature is made of a representative material, and boundary conditions, such as maintaining natural tissue tension and appropriate consideration of the influence of the subcutaneous layer on microneedle penetration. Whilst Moronkeji et al. (2017) utilised gelatine to represent fat and Perma-Gel for muscle in their microneedle penetration tests, Kochhar et al. (2013) [57] demonstrated that PDMS has mechanical properties in close resemblance to inherent subcutaneous tissues. Indeed, in the work performed here, the PDMS sheeting upon which the skin was pinned reflected comparable data between *in vivo* and *ex vivo* in penetration depths.

4.2. Penetration depths of microprojections affected during post mortem

Penetration depth correlated with the drop of elastic modulus in some, but not all pigs. This large scatter of data is observed in biological tissues, including mouse skin (Kendall et al., 2007; Crichton et al., 2013) and pigs (Wei et al., 2017). This change in depth ultimately affects where the payload will be deposited (cf. skin layer thicknesses Fig. 7 (b–d)). The most prominent reduction was between *in vivo* and immediately post-death *in situ* skin – the immediate reduction of pressure due to blood circulation cut off may have softened the dermis, as well as muscle tissue. This decreased stiffness of deep layers may thus inhibit resultant penetration of microprojections. Contradicting findings were concluded by Gefen and Margulies and Prevost et al. (2011), although in porcine brains, the pressurised vasculature seems to contribute less to the tissue mechanical properties. We think this could be because the cerebral blood volume (CBV) of blood in pigs is a small fraction in pigs, ~2–6% (Østergaard et al., 1998), and that blood volume in muscle tissues would be significantly higher, at ~25% of the cardiac output at rest (Ng et al., 2012).

4.3. Specific changes in penetration depths and delivery efficiencies observed during rigor mortis

In contrast to the softening of tissues observed *post mortem*, the stiffening of muscle tissue in instances when *rigor mortis* was witnessed in some pigs saw increased in penetration depths and delivery efficiencies, despite experimenting indoors with controlled temperatures to minimise variation to *rigor mortis* onset, which is ambient temperature dependent (Krompecher, 1981). This effect is most likely the cause of the bimodal scatter in the penetration depths and delivery efficiency of 240 min time point, although Gefen and Margulies (2004) were uncertain of the extent of the *rigor mortis* effect on mechanical properties. In this study, however, stiffer tissue layers may have a direct impact by reflecting the impact forces during patch application, thereby compressing the skin tissue further and allowing deeper engagement of the projections, allowing more portion of the formulation releasing into the skin.

An increasing trend of delivery efficiency of coating formulations was observed across the time points, which may explain the correlation with *rigor mortis*, measured elasticity, and penetration depth, it is a possibility that a relatively low delivery efficiency at the *in vivo* phase (even though penetration was deeper) suggests a systemic circulation during the *in vivo* state could play a role in the clearance of formulation away from the skin, as the skin was only excised at the end of the total elapsed time to keep the area intact. The percentage of the dose delivered – using the same gas-jet coating method – has been similarly reported in previous Nanopatch application studies (0.1–16.5%) (Pearson et al., 2013). Alternative coating methods (e.g. dip coating) produce much higher delivery efficiencies (e.g. >85% (Chen et al. 2010) [36]).

4.4. Visual observations of erythema after patch application

As shown in the erythema photos in Fig. 4(d–h), in some cases microprojections induced inflammation of the skin. If this is a sign of capillary leakage when the penetration depth was approximately 100 μm, then it suggests that potential access of blood capillaries with the Nanopatch, opening up future applications in diagnostics, beyond drug delivery (Coffey et al., 2016, 2018). An increasing delivery efficiency even prior to *rigor mortis* may be explained by the open microchannels created by the microprojections, where formulations remained on the skin surface may diffuse through the skin. Certainly, as shown by Haridass and Wei et al. (Haridass et al., 2019), the pores remain open for up to 48 h. Another probable cause of low delivery efficiency may be due to the excision of patched sites only after the conclusion of the experiment, and that the ^{14}C labelled ovalbumin (~45 kDa) (Abeyrathne et al., 2013) may have already diffused significantly away from the patched site. As explored by Wei and Haridass et al. (Wei et al., 2018), rapid clearance of rhodamine dextran in *ex vivo* human skin was observed for the 70 kDa-sized molecules upon imaging (the cells of freshly-excised human skin are likely still viable for formulation interaction). The quantification of the remaining ^{14}C on the patch may not necessarily be an accurate indication of the delivered dose, as the amount of ^{14}C coated on each patch are not identical.

4.5. Device performance and quality (scatter) of data with respect to microprojection design, skin layers, skin model and application methods

Higher spread of penetration depth was observed in the dermis penetration data, compared with lower patch application speeds that did not reach the dermis, might be due to looser dermal collagen network, allowing easier penetration of microprojections into the papillary dermis once the dermal-epidermal junction is breached. The range of velocities investigated in the *ex vivo* study also identified the settings for the skin layer desired to be targeted. For example, on the porcine skin, an application speed of 8–12 m s^{-1} will primarily deposit the formulations into the viable epidermis, while at speeds above 16 m s^{-1}, both the

viable epidermis and the papillary dermis will be targeted. Similarities of pig skin and human skin morphologies are commented by researchers (Jacobi et al., 2007), although the elasticity of the human skin is significantly lower than pig skin, as explored by Wei et al. (2017). Human skin may thus require much higher speeds – or higher application energy delivered by different means or geometries (Crichton et al., 2016; Meliga et al., 2017) – to achieve the equivalent penetration depth and delivery. Changing the projection geometry as opposed to increasing the application speed also allows for deeper skin penetration and thereby increasing the delivery efficiency was recently reported in Crichton et al.'s study (Crichton et al., 2016). In addition, Kerdok et al. (2006) reported that in the absence of perfusion, *ex vivo* liver is less viscoelastic compared with *in vivo* liver, and as proposed by Wei et al. (2017), the viscoelasticity of human skin is less than that of pigs, which would suggest less pronounced differences between *in vivo* and *ex vivo* conditions, than other animal models would. *Ex vivo* conditions would also effectively eliminate the transient change in mechanical properties due to *rigor mortis*.

4.6. Substrates of skin model affecting microprojection device performance

Correlation between delivery efficiency, penetration depth with tissue elasticity, due to blood circulation and *rigor mortis*, up to this point have been discussed. However, just how much is this affecting functional medical device attributes? Maximum bulk displacement of the skin was approximately 5 mm deep due to a patch application (Supplementary Fig. 2). Using the "10% rule of thumb" in indentation, as already explored and used in Wei et al. (2017) for indentation, suggesting that up to 50 mm of tissue beneath the skin surface could contribute to the overall elasticity measured. However, Cartmill (Chao et al., 2010) commented that in a homogenous, synthetic skin model, perturbation waves attenuated well before reaching the 10% depth. Indeed, this was shown in a side experiment that the critical relative indentation depth, a depth at which indentation tests start to measure the effects of the substrate rather than the material, of PDMS at a very compliant 20:1 ratio is likely around 30% (Supplementary Fig. 2) (Bartali et al., 2014). The patch size to tissue thickness (including all soft tissues) ratio is also well less than unity as proposed by Hayes et al. for tissue characterisation (Hayes et al., 1972). Nonetheless, non-invasive, highly dynamic testing methods would invariably capture deeper tissue layers and would be more difficult to isolate. Therefore, substrates beneath the skin for *in vivo* and *in situ* models must also be considered, which includes, adipose tissues, muscle and bone, and would affect the consistency of patch application. In a clinical sense, the application site of each patient would, therefore, be significantly different. The inguinal bulk, dynamic, tissue elastic modulus is significantly higher (~5–15 kPa) than that of rump (~15–60 kPa) (Fig. 3). Skin thicknesses between the two sites were different (Fig. 7(b–d)), but evidently a smaller difference than fat and muscle tissue thicknesses at the two sites. For improved and more streamlined functional medical device development, a more controlled *ex vivo* state would mitigate this variability, as shown in Supplementary Fig. 1. Boundary conditions imposed on the *ex vivo* setup may also explain similarities in penetration depth with the *in vivo* condition, as the skin was pinned back to its original shape and subcutaneous tissues were also replicated.

4.7. Applicator device performance

The maximum velocity of the applicator device is 16 m s^{-1}. We detuned the velocities to 8 and 12 m s^{-1} in Fig. 7 (a) to explore if payload delivery depth could be controlled, and it appears that within the range it is possible. Although, we believe that a speed that is "too low" may negatively affect penetration depth, as the skin is viscoelastic, and at low strain rates, it will most likely tend to deflect than to allow microneedles to puncture. We suggest that increasing the velocity and decreasing the mass (while allowing the energy to remain the same) may yield more consistent delivery.

4.8. Limitations and future work

Firstly, we acknowledge that in this paper, we used a specific, commercial (prototype) device – the Nanopatch – as an "off-the-shelf" tool and a representation of a class of soft-tissue interfacing microneedle devices, with similar methods of application (e.g. energy/velocity with an applicator device) and scale of microneedle structures (e.g. width, length, density). We do believe that using similar alternatives would yield similar results (subject to the aforementioned factors). Secondly, data gathered in this study was limited to only five pigs, three of them extended to 240 min time point, and only the first four underwent skin elasticity evaluation *in vivo* and *in situ*. Three skin specimens were harvested from three different pigs for *ex vivo* testing. Although the scatter and consistency of the data were discussed above, further testing would provide more evidence to support this study. Thirdly, future experiments could explore longer time points post *rigor mortis in situ* and delivery efficiency *ex vivo*, although whether the results obtained for these conditions are useful to researchers for device evaluation are unknown. Fourthly, despite the similarities between human and porcine skin (Wei et al., 2017) (and the site of the skin), there are still intrinsic differences between the two (i.e. lower elasticity and viscoelasticity in humans), so we suggest looking at the relative changes reported herein, rather than the absolute values. Fifthly, future work could investigate increasing the application velocity and decreasing the system mass, with a focus on energy applied per microneedle. Finally, other measurement techniques could also be used to complement the current indicators used for device performance evaluation, namely, penetration depth and delivery efficiency.

4.9. Discussion summary

Concluding from the results obtained in this study, the testing of medical devices *in vivo* should avoid the period of *rigor mortis*. *In vivo* conditions would be the most representative, although scatter for different tissue substrates beneath the skin should be considered. Attention should also be given to systemic circulation for the delivery of small molecules *in vivo*, as transport of molecules would effectively reduce delivery efficiency and also provide additional pressure in tissue stiffness. *Ex vivo* conditions offered consistent results and are recommended after *in vivo* models should animal or human experimentation not be possible.

5. Conclusion

Animal models of the skin are key to the development of microdevices, but to date, there has not been data to help understand how microdevices could perform different with *in vivo, in situ* or *ex vivo* models. This study examined two main quantifiable techniques – delivery efficiency and penetration depth in a porcine model. Together, we found the higher elastic modulus of porcine skin (with underlying tissues), lead to higher penetration depths of the Nanopatch. This was observed during *in vivo* and *rigor mortis in situ* conditions. Delivery efficiency did not appear to correlate with tissue stiffness nor penetration depth but did correlate inversely with elapsed time since patching. An *ex vivo* boundary condition was implemented and tested to resemble *in vivo* conditions, which could be used when *in vivo* experimentation is not possible, including the advantage of isolating substrate effects. We believe the data obtained is here is useful for those developing devices, modelling tissue behaviour and for a wider consideration of medical device applications.

Data availability

The datasets generated and/or analysed during the current study are available from the corresponding author on reasonable request.

Contributions

JCJW: conceptualisation, data curation, formal analysis, funding acquisition, investigation, methodology, project administration, software, validation, visualisation, writing – original draft, writing – review & editing. IDC: conceptualisation, data curation, formal analysis, investigation, methodology, project administration, software, validation, visualisation, writing – original draft, writing – review & editing. MAFK: conceptualisation, funding acquisition, resources, supervision, validation, writing – review & editing. MLC: conceptualisation, funding acquisition, investigation, methodology, supervision, validation, writing – review & editing.

CRediT authorship contribution statement

Jonathan CJ. Wei: Conceptualization, Data curation, Formal analysis, Funding acquisition, Investigation, Methodology, Project administration, Software, Validation, Visualization, Writing – original draft, Writing – review & editing. **Ian D. Cartmill:** Writing – review & editing, Writing – original draft, Visualization, Validation, Software, Project administration, Methodology, Investigation, Formal analysis, Data curation, Conceptualization. **Mark AF. Kendall:** Funding acquisition, Resources, Supervision, Validation, Writing – review & editing, Conceptualization. **Michael L. Crichton:** Writing – review & editing, Validation, Supervision, Methodology, Investigation, Funding acquisition, Conceptualization.

Declaration of competing interest

The authors declare the following financial interests/personal relationships which may be considered as potential competing interests:

JCJW and MLC both worked on the technology as UQ employees funded by Vaxxas (a company commercialising the technology) prior to commencing on this work. MAFK is the founder of Vaxxas and was the Vaxxas Chief Technology Officer, Company Director and Chair of the Vaxxas Advisory Board. The Nanopatch technology has been licensed by UQ to Vaxxas for commercialisation. There has been no financial support for this work that could have influenced its outcome.

Acknowledgements

We would like to thank the UQ staff (Dr Cora Lau, Tanya McKenna, Milou Dekkers, Andrew Kelly, Walter Steginga, Blair McEwan, Sean O'Loughlin) and Vaxxas staff (Dr Angus Förster, Dr César Jayashi) for helping us with organising and carrying out the study. This work was supported through the Australian Research Council Centre of Excellence in Convergent Bio-Nano Science & Technology Grant (CE140100036), the Australian Research Council Grant (DP1093281). JCJW is a recipient of the Australian Government Research Training Program Scholarship and the AIBN top up scheme. This work was performed in part at the Australian National Fabrication Facility Queensland Node, a company established under the National Collaborative Research Infrastructure Strategy to provide nano- and micro-fabrication facilities for Australia's Researchers.

Appendix A. Supplementary data

Supplementary data to this article can be found online at https://doi.org/10.1016/j.jmbbm.2022.105187.

References

Abeyrathne, E.D.N.S., Lee, H.Y., Ahn, D.U., 2013. Egg white proteins and their potential use in food processing or as nutraceutical and pharmaceutical agents–a review. Poultry Sci. 92, 3292–3299.
Bartali, R., et al., 2014. Critical relative indentation depth in carbon based thin films. Prog. Nat. Sci.: Mater. Int. 24, 287–290.
Bilston, L.E., 2002. The effect of perfusion on soft tissue mechanical properties: a computational model. Comput. Methods Biomech. Biomed. Eng. 5, 283–290.
Birchall, J.C., 2006. Microneedle array technology: the time is right but is the science ready? Expet Rev. Med. Dev. 3, 1–4.
Brooks, J.W., 2016. Postmortem changes in animal carcasses and estimation of the postmortem interval. Vet. Pathol. 53, 929–940.
Brown, J.D., et al., 2003. In-vivo and in-situ compressive properties of porcine abdominal soft tissues. Stud. Health Technol. Inf. 94, 26–32.
Cartmill, Ian D., 2014. Dynamic Mechanical Interaction between Solid Projections and Skin: Impact and Surface Perturbations. The University of Queensland.
Chao, C.Y.L., Zheng, Y.P., Huang, Y.P., Cheing, G.L.Y., 2010. Biomechanical Properties of the Forefoot Plantar Soft Tissue as Measured by an Optical Coherence Tomography-Based Air-Jet Indentation System and Tissue Ultrasound Palpation System. https://doi.org/10.1016/j.clinbiomech.2010.03.008.
Chen, X., et al., 2009. Dry-coated microprojection array patches for targeted delivery of immunotherapeutics to the skin. J. Contr. Release 139, 212–220.
Chen, X., et al., 2010. Site-selectively coated, densely-packed microprojection array patches for targeted delivery of vaccines to skin. Adv. Funct. Mater. 21, 464–473.
Chen, X., et al., 2012. Rapid kinetics to peak serum antibodies is achieved following influenza vaccination by dry-coated densely packed microprojections to skin. J. Contr. Release 158, 78–84.
Coffey, J.W., Meliga, S.C., Corrie, S.R., Kendall, M.A.F., 2016. Dynamic application of microprojection arrays to skin induces circulating protein extravasation for enhanced biomarker capture and detection. Biomaterials 84, 130–143.
Coffey, J.W., Corrie, S.R., Kendall, M.A.F., 2018. Rapid and selective sampling of IgG from skin in less than 1 min using a high surface area wearable immunoassay patch. Biomaterials 170, 49–57.
Crichton, M.L., et al., 2010. The effect of strain rate on the precision of penetration of short densely-packed microprojection array patches coated with vaccine. Biomaterials 31, 4562–4572.
Crichton, M.L., Chen, X., Huang, H., Kendall, M.A.F., 2013. Elastic modulus and viscoelastic properties of full thickness skin characterised at micro scales. Biomaterials 34, 2087–2097.
Crichton, M.L., et al., 2016. The changing shape of vaccination: improving immune responses through geometrical variations of a microdevice for immunization. Sci. Rep. 6, 27217.
Davey, C.L., Gilbert, K.V., Carse, W.A., 1976. Carcass electrical stimulation to prevent cold shortening toughness in beef. N. Z. J. Agric. Res. 19, 13–18.
Fernando, G.J.P., et al., 2016. Influenza nucleoprotein DNA vaccination by a skin targeted, dry coated, densely packed microprojection array (Nanopatch) induces potent antibody and CD8(+) T cell responses. J. Contr. Release 237, 35–41.
Fernando, G.J.P., et al., 2018. Safety, tolerability, acceptability and immunogenicity of an influenza vaccine delivered to human skin by a novel high-density microprojection array patch (Nanopatch™). Vaccine 36, 3779–3788.
Gefen, A., Margulies, S.S., 2004. Are in vivo and in situ brain tissues mechanically similar? J. Biomech. 37, 1339–1352.
Goddard, R.W., Kendall, M.A.F., Meliga, S., 2018. Microprojection Arrays with Enhanced Skin Penetrating Properties and Methods Thereof.
Groves, R.B., Coulman, S.A., Birchall, J.C., Evans, S.L., 2012. Quantifying the mechanical properties of human skin to optimise future microneedle device design. Comput. Methods Biomech. Biomed. Eng. 15, 73–82.
Guan, Y., et al., 2014. Optical tracking of local surface wave for skin viscoelasticity. Med. Eng. Phys. 36 (6), 708–714.
Guertler, C.A., et al., 2018. Mechanical properties of porcine brain tissue in vivo and ex vivo estimated by MR elastography. J. Biomech. 69, 10–18.
Haridass, I.N., et al., 2019. Cellular metabolism and pore lifetime of human skin following microprojection array mediation. J. Contr. Release 306, 59–68.
Hayes, W.C., Keer, L.M., Herrmann, G., Mockros, L.F., 1972. A mathematical analysis for indentation tests of articular cartilage. J. Biomech. 5, 541–551.
Huang, Y.-P., et al., 2009. An optical coherence tomography (OCT)-based air jet indentation system for measuring the mechanical properties of soft tissues. Meas. Sci. Technol. 20, 1–11.
Jacobi, U., et al., 2007. Porcine ear skin: an in vitro model for human skin. Skin Res. Technol. 13, 19–24.
Jenkins, D., Corrie, S., Flaim, C., Kendall, M., 2012. High Density and High Aspect Ratio Solid Micro-nanoprojection Arrays for Targeted Skin Vaccine Delivery and Specific Antibody Extraction. https://doi.org/10.1039/C2RA20153D.
Kendall, M., Mitchell, T., Wrighton-Smith, P., 2004a. Intradermal ballistic delivery of micro-particles into excised human skin for pharmaceutical applications. J. Biomech. 37, 1733–1741.
Kendall, M., Rishworth, S., Carter, F., Mitchell, T., 2004b. Effects of relative humidity and ambient temperature on the ballistic delivery of micro-particles to excised porcine skin. J. Invest. Dermatol. 122, 739–746.
Kendall, M., Rishworth, S., Carter, F., Mitchell, T., 2004c. Effects of relative humidity and ambient temperature on the ballistic delivery of micro-particles to excised porcine skin. J. Invest. Dermatol. 122 (3), 739–746. https://doi.org/10.1111/j.0022-202X.2004.22320.x.PMID:15086561. Mar.

Kendall, M.A.F., Chong, Y.-F., Cock, A., 2007. The mechanical properties of the skin epidermis in relation to targeted gene and drug delivery. Biomaterials 28, 4968–4977.
Kerdok, A.E., Ottensmeyer, M.P., Howe, R.D., 2006. Effects of perfusion on the viscoelastic characteristics of liver. J. Biomech. 39, 2221–2231.
Kirkpatrick, S.J., Duncan, D.D., Fang, L., 2004. Low-frequency surface wave propagation and the viscoelastic behavior of porcine skin. J. Biomed. Opt. 9 (6), 1311–1319.
Kochhar, J., et al., 2013. Effect of microneedle geometry and supporting substrate on microneedle array penetration into skin. J. Pharmaceut. Sci. 102, 4100–4108.
Krompecher, T., 1981. Experimental evaluation of rigor mortis V. Effect of various temperatures on the evolution of rigor mortis. Forensic Sci. Int. 17, 19–26.
Li, S., Oldenburg, A.L., 2011. Measuring Soft Tissue Elasticity By Monitoring Surface Acoustic Waves Using Image Plane Digital Holography. Proceedings Volume 7965, Medical Imaging 2011: Biomedical Applications in Molecular, Structural, and Functional Imaging, p. 79652M. https://doi.org/10.1117/12.883254.
Li, C., et al., 2011. Determining elastic properties of skin by measuring surface waves from an impulse mechanical stimulus using phase-sensitive optical coherence tomography. J. R. Soc. Interface 9 (70), 831–841. May 7.
Lister, K., Gao, Z., Desai, J.P., 2011. Development of in vivo constitutive models for liver: application to surgical simulation. Ann. Biomed. Eng. 39, 1060–1073.
Manfredi, L.R., et al., 2012. The effect of surface wave propagation on neural responses to vibration in primate glabrous skin. PLoS One 7 (2), e31203.
Meliga, S.C., et al., 2017. The hyperelastic and failure behaviors of skin in relation to the dynamic application of microscopic penetrators in a murine model. Acta Biomater 48, 341–356.
Moronkeji, K., Todd, S., Dawidowska, I., Barrett, S., Akhtar, R., 2017. The role of subcutaneous tissue stiffness on microneedle performance in a representative in vitro model of skin. J. Contr. Release 265, 102–112.
Muller, D.A., et al., 2016. Inactivated poliovirus type 2 vaccine delivered to rat skin via high density microprojection array elicits potent neutralising antibody responses. Sci. Rep. 6, 22094.
Muller, D.A., et al., 2017. High-density microprojection array delivery to rat skin of low doses of trivalent inactivated poliovirus vaccine elicits potent neutralising antibody responses. Sci. Rep. 7, 12644.
Ng, H.-I., Fernando, G.J.P., Kendall, M.A.F., 2012. Induction of potent $CD8^+$ T cell responses through the delivery of subunit protein vaccines to skin antigen-presenting cells using densely packed microprojection arrays. J. Contr. Release 162, 477–484.
Østergaard, L., et al., 1998. Absolute cerebral blood flow and blood volume measured by magnetic resonance imaging bolus tracking: comparison with positron emission tomography values. J. Cerebr. Blood Flow Metabol. 18, 425–432.
Pearson, F.E., et al., 2013. Dry-coated live viral vector vaccines delivered by nanopatch microprojections retain long-term thermostability and induce transgene-specific T cell responses in mice. PLoS One 8, e67888.
Prevost, T.P., et al., 2011. Dynamic mechanical response of brain tissue in indentation in vivo, in situ and in vitro. Acta Biomater 7, 4090–4101.
Raphael, A.P., et al., 2013. Depth-resolved characterization of diffusion properties within and across minimally-perturbed skin layers. J. Contr. Release 166, 87–94.
Shankar, N., et al., 2014. Influence of skin-to-muscle and muscle-to-bone thickness on depth of needle penetration in adults at the deltoid intramuscular injection site. Med. J. Armed Forces India 70, 338–343.
Wei, J.C.-J., 2018. The Key Biomechanics of the Skin for the Translation of Microscale Medical Devices from Animal Models to Humans. The University of Queensland.
Wei, J.C.J., et al., 2017. Allometric scaling of skin thickness, elasticity, viscoelasticity to mass for micro-medical device translation: from mice, rats, rabbits, pigs to humans. Sci. Rep. 7, 15885.
Wei, J.C.J., et al., 2018. Space- and time-resolved investigation on diffusion kinetics of human skin following macromolecule delivery by microneedle arrays. Sci. Rep. 8, 17759.
Zhang, X., Greenleaf, J.F., 2007. Estimation of tissue's elasticity with surface wave speed. J. Acoust. Soc. Am. 122 (5), 2522–2525.
Zhang, X., Qiang, B., Greenleaf, J., 2011. Comparison of the surface wave method and the indentation method for measuring the elasticity of gelatin phantoms of different concentrations. Ultrasonics 51 (2), 157–164.